Mon. Not. R. Astron. Soc. **000**, 1–15 (2010) Printed 28 May 2010 (MN LaTeX style file v2.2)

Can one reconstruct masked CMB sky?

R. Aurich and S. Lustig
Institut für Theoretische Physik, Universität Ulm,
Albert-Einstein-Allee 11,
D-89069 Ulm, Germany

ABSTRACT
The CMB maps obtained by observations always possess domains which have to be masked due to severe uncertainties with respect to the genuine CMB signal. Cosmological analyses ideally use full CMB maps in order to get e. g. the angular power spectrum. There are attempts to reconstruct the masked regions at least at low resolutions, i. e. at large angular scales, before a further analysis follows. In this paper, the quality of the reconstruction is investigated for the ILC (7yr) map as well as for 1000 CMB simulations of the ΛCDM concordance model. The latter allows an error estimation for the reconstruction algorithm which reveals some drawbacks. The analysis points to errors of the order of a significant fraction of the mean temperature fluctuation of the CMB. The temperature 2-point correlation function $C(\vartheta)$ is evaluated for different reconstructed sky maps which leads to the conclusion that it is safest to compute it on the cut-sky.

Key words: Methods: data analysis, statistical; Cosmology: cosmic microwave background, large-scale structure of Universe

1 INTRODUCTION

The cosmic microwave background (CMB) provides one of the cornerstones of the cosmological concordance model. The statistical properties of our cosmological models have to match those of the CMB in order to give an admissible model. Thus, it is of utmost importance to reliably extract the statistical properties of the CMB. A main obstacle is the foreground emission of our galaxy and of other sources which restrict the area of the sky available for a sufficiently clean CMB signal, i. e. the full sky CMB signal has to be masked. One path of statistical analysis leads to the Fourier space in which the CMB is decomposed with respect to spherical harmonics $Y_{lm}(\hat{n})$ where the masked sky leads to a coupling between the Fourier modes since no full sky CMB is available. In this paper, we do not delve into these difficulties, where upon an extensive literature exists, but instead follow the alternative path which allows an analysis directly in the pixel space, which in turn is more adapted to a masked sky. This analysis is based on the temperature two-point correlation function $C(\vartheta)$, which is defined as

$$C(\vartheta) \;:=\; \left\langle \delta T(\hat{n}) \delta T(\hat{n}') \right\rangle \quad \text{with} \quad \hat{n}\cdot\hat{n}' = \cos\vartheta \quad , \qquad (1)$$

where $\delta T(\hat{n})$ is the temperature fluctuation in the direction of the unit vector $\hat{n}$. The most direct way to deal with a mask is just to use only those pixels which are outside the mask. In this way it was discovered by the COBE team (Hinshaw et al. 1996) that the correlation function $C(\vartheta)$ possesses surprisingly low power at large angles $\vartheta \gtrsim 60°$.

A surprising observation is made by using the ILC map, which represents a full sky CMB map obtained by the WMAP team (Gold et al. 2010). Computing the correlation function $C(\vartheta)$ using a mask leads to a correlation function having very low power at large scales, whereas using the complete ILC map leads to a correlation function which possesses higher large scale power being compatible with the concordance model (Spergel et al. 2003). One has to decide which correlation function $C(\vartheta)$ corresponds to the true CMB sky: the one which is based on the safe pixels, i. e. those outside the mask, or the other one, which would imply that most of the large scale power is generated by those areas hidden by the galaxy, i. e. by those pixels which have experienced much larger corrections. This question has recently stimulated much discussions, e. g. (Copi et al. 2007, 2009, 2010; Hajian 2007; Aurich et al. 2008, 2010; Sarkar et al. 2010; Bennett et al. 2010; Efstathiou et al. 2009; Pontzen and Peiris 2010).

Efstathiou et al. (2009) emphasise that one has to start with the cut sky, but before the correlation function $C(\vartheta)$ is computed the low-order multipoles have to be reconstructed. In this way, a stable result is obtained as long as the mask is not too large. The obtained correlation function is then the one with large power at large scales. For the details of the method see de Oliveira-Costa and Tegmark (2006); Bielewicz et al. (2004). Here we summarise only the most important ingredients. The data vector $\vec{x}$ containing only the pixel values outside the mask is related to the spherical

harmonic coefficients a_{lm} represented as $\vec{a}$ by

$$\vec{x} \;=\; Y\,\vec{a} + \vec{n} \quad , \tag{2}$$

where Y_{ij} denotes the corresponding values of $Y_{l_j m_j}(\hat{n}_i)$ and $\vec{n}$ the noise. In the low-order multipole reconstruction, only the multipoles with $l \leqslant l_{\max} = 10 \ldots 20$ are taken into account. The methods of reconstruction differ by the choice of a square matrix A which determines the reconstructed $\vec{a}^{\,r}$ by

$$\vec{a}^{\,r} \;=\; (Y^T A Y)^{-1}\, Y^T A \vec{x} \quad . \tag{3}$$

Setting the matrix A equal to the unit matrix leads to the method of "direct inversion". To take the correlations between the pixels into account, one can choose the covariance matrix $A^{-1} =< \vec{x} \cdot \vec{x}^{\,T} >$ for a reconstruction up to $l_{\max}$, which leads to the method used by de Oliveira-Costa and Tegmark (2006) with

$$A^{-1}_{ij} \;=\; \sum_{l=l_{\max}+1}^{l_{\rm cut}} \frac{2l+1}{4\pi}\, P_l(\hat{n}_i \cdot \hat{n}_j)\, C_l \tag{4}$$

ignoring the noise contribution. The sum in (4) runs only over those multipole moments C_l, $l > l_{\max}$, that are not to be reconstructed.

The reconstructed sky map up to $l_{\max}$ is then obtained from the coefficients $\vec{a}^{\,r}$. Efstathiou et al. (2009) compute the correlation function $C(\vartheta)$ from such reconstructed maps for $l_{\max} = 5$ to $l_{\max} = 20$ by using the KQ85 or the KQ75 mask provided by the WMAP team, and it is found that these $C(\vartheta)$ only show a negligible variation. This is interpreted as a sign for a stable method to compute the temperature correlation in the presence of masks. It should be emphasised that the WMAP team bases its 7 year investigation with respect to CMB anomalies (Bennett et al. 2010) on the method of (Efstathiou et al. 2009). This leads to the conclusion that the correlation function agrees well with the ΛCDM concordance model and displays thus no anomalous behaviour.

The system of equations (3) is over-determined, since there are much more pixel values than multipole moments with $l \leqslant l_{\max}$ as long as the mask and $l_{\max}$ are not too large. Thus, there is the hope that the pixels outside the mask already determine the low-order multipoles. The caveat in the demonstration of (Efstathiou et al. 2009) is, however, that a large Gaussian smoothing of 10° is applied to the maps *before* the cut is applied. Due to this smoothing there is a transfer of information from pixel values within the mask to those outside the mask. Since the system of equations (3) is already over-determined, this additional information is readily extracted and reveals the temperature structure within the mask after the "reconstruction". It should be noted that even a downgrade in the HEALPix resolution can lead to an information transfer by carrying out the downgrade before the mask is applied.

The two masks used in this paper are the KQ85 (7yr), shown in figure 1a, and the KQ75 (7yr) mask which are available at the LAMBDA website. These are stored in the HEALPix (Górski et al. 2005) format with a HEALPix resolution of $N_{\rm side} = 512$. The reconstruction algorithm requires masks in lower resolutions of $N_{\rm side} = 16$ or 32, and a downgrade has to be carried out. A single downgraded pixel i contains $N_{\rm total}$ pixels of the higher resolution map and from these only $N_{\rm nm}$ pixel values are used in the averaging process, i. e. those that are *not* masked in the higher resolution map, in order to compute the value of the downgraded pixel. If the ratio

$$x(i) \;=\; \frac{N_{\rm nm}}{N_{\rm total}} \tag{5}$$

is larger than a given mask threshold $x_{\rm th} \in (0.0, 1.0)$, i. e. $x(i) > x_{\rm th}$, the resulting pixel is *not* masked, and otherwise it is masked. The result of the KQ85 (7yr) mask for $N_{\rm side} = 16$ and $x_{\rm th} = 0.5$ is shown in figure 1b. It is obvious that the size of the masked domains in masks with $N_{\rm side} < 512$ depends on this mask threshold $x_{\rm th}$.

(a) KQ85 (7yr) mask, $N_{\rm side} = 512$

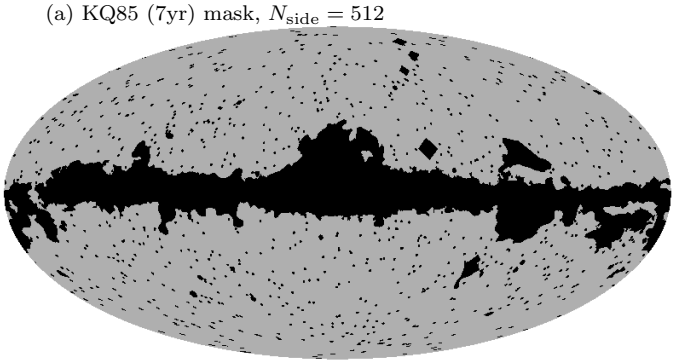

(b) KQ85 (7yr) mask, $N_{\rm side} = 16$, $x_{\rm th} = 0.5$

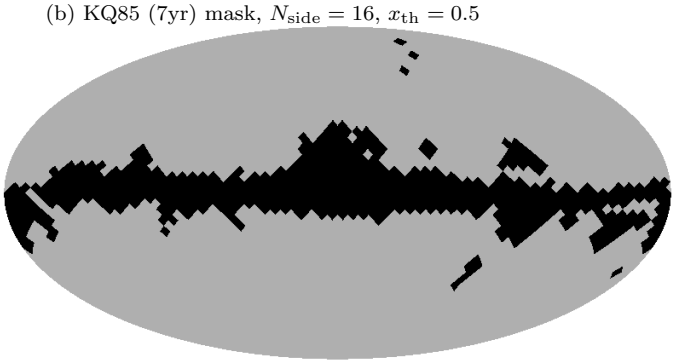

Figure 1. The KQ85 mask of the WMAP 7 year data with a pixel resolution of $N_{\rm side} = 512$ is displayed in panel 1a. The masked region is pictured in black. Figure 1b shows the KQ85 mask downgraded to a pixel resolution of $N_{\rm side} = 16$. All pixels with $x(i) \leqslant 0.5$, equation (5), are considered as masked.

In the next sections we will compare results of CMB simulations of the ΛCDM concordance model with those of the ILC map. For this reason all maps of the ΛCDM concordance model are produced in a FWHM resolution of 1° and $N_{\rm side} = 512$. But we also investigate these maps and the ILC map after an additional smoothing of e. g. 10°. In the following only the additional smoothing width is specified.

Let us now return to the information transfer caused by the smoothing procedure and/or by carrying out the downgrade. The following simple numerical experiment presented in figures 2 and 3 reveals the information transfer. Figure 2a displays the CMB simulation A of the ΛCDM concordance model after a smoothing of 10°. This map is downgraded from a pixel resolution of $N_{\rm side} = 512$ to $N_{\rm side} = 16$. Then the KQ85 mask in the pixel resolution $N_{\rm side} = 16$, shown in figure 1b, is applied. For $l_{\max} = 10$ the reconstruction algorithm (3) is used to obtain the reconstructed map shown

(a) ΛCDM simulation A

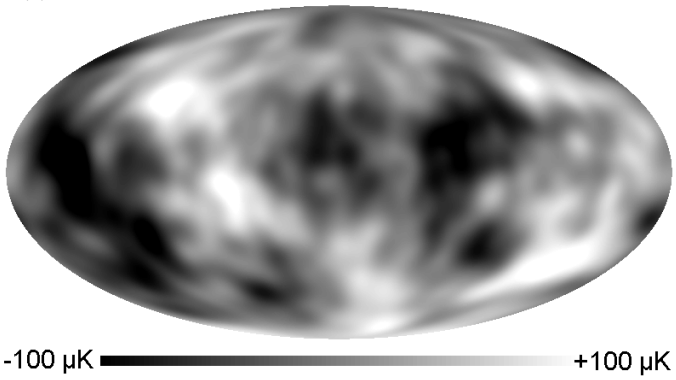

(b) ΛCDM simulation B

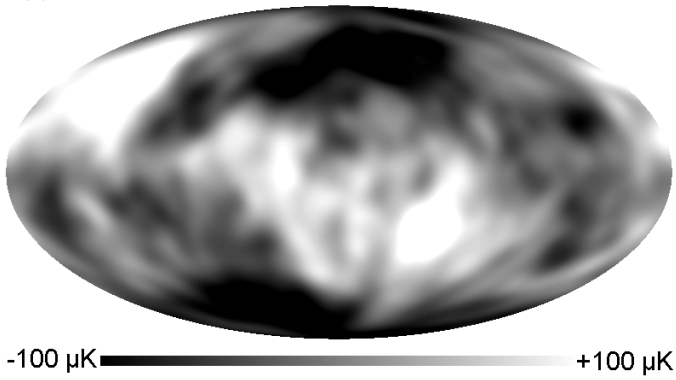

(c) ΛCDM simulation A outside and B inside KQ85 mask

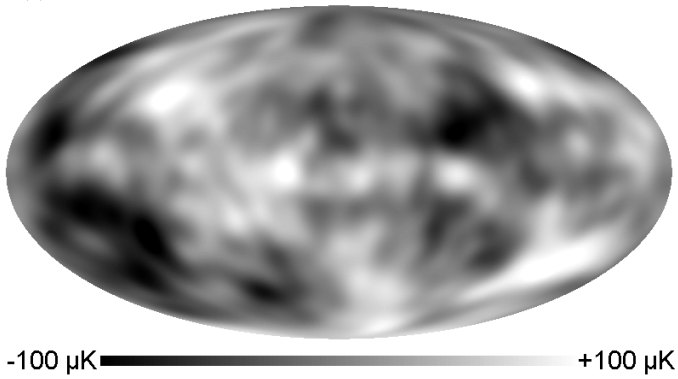

Figure 2. Figure 2a shows the CMB simulation A of the ΛCDM concordance model with a pixel resolution of $N_{\rm side} = 512$ and an additional smoothing of 10°. In figure 2b a second map (CMB simulation B) using the same cosmological parameters is displayed. The map in figure 2c results from the models used for figure 2a and 2b where the pixels outside the KQ85 mask are taken from simulation A and inside from simulation B at the resolution $N_{\rm side} = 512$. Thereafter a Gaussian smoothing of 10° is applied.

(a) ΛCDM simulation A

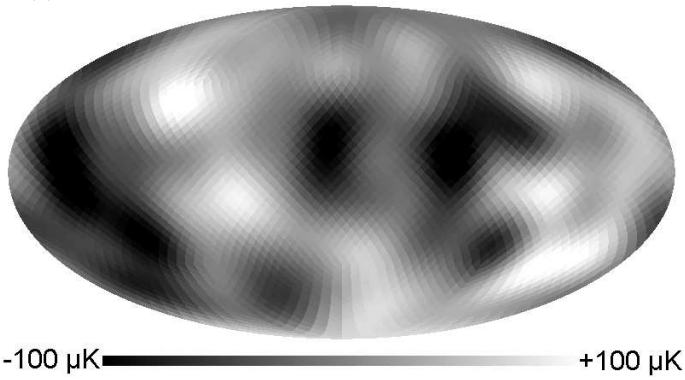

(b) ΛCDM simulation B

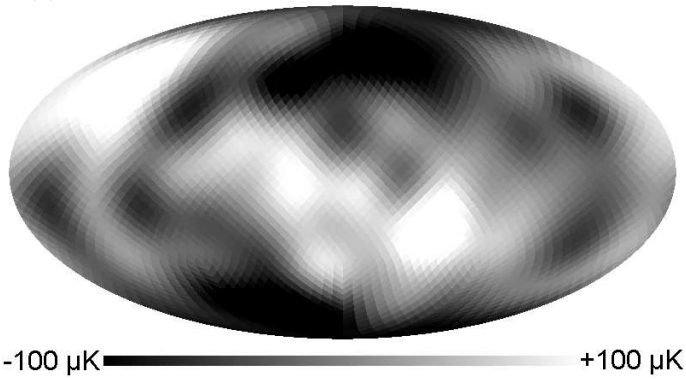

(c) ΛCDM simulation A outside and B inside KQ85 mask

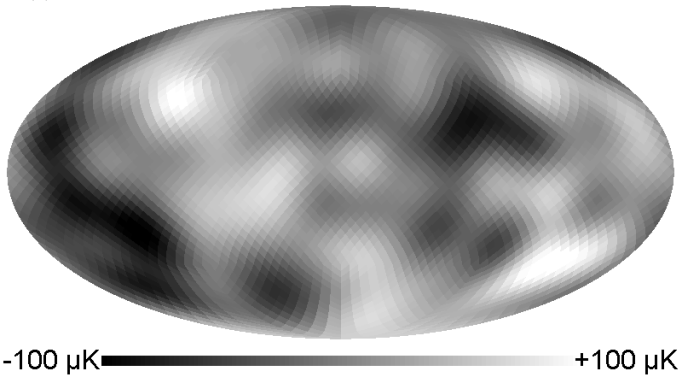

Figure 3. The three reconstructed maps are displayed. The reconstructions are carried out for $l_{\rm max} = 10$. These maps result from the maps in figure 2a, b and c by downgrading these maps to a pixel resolution of $N_{\rm side} = 16$ and thereafter applying the reconstruction algorithm (3) to the data outside the mask shown in figure 1b. Note that panel (a) and (c) should show the same sky map if the reconstruction algorithm would not use information from the masked region. However, there are significant difference especially near the Galactic plane.

in figure 3a. Both the original and the reconstructed map agree within the mask reasonably well. The same procedure is repeated for a second simulation B where figure 2b shows the simulation and figure 3b the reconstruction. In the next step the pixels of simulation A are replaced at a pixel resolution of $N_{\rm side} = 512$ within the KQ85 mask, shown in figure 1a, by those of simulation B shown in figure 2b. After this replacement the smoothing of 10° is applied. The last step transfers now the "wrong" information to the pixels outside the mask. This smoothed map is shown in figure 2c. Downgrading this map to $N_{\rm side} = 16$ provides the data outside the mask which are used for the reconstruction. If the reconstruction would not use the information within the mask, the reconstructed map of figure 3a should reappear. However, as revealed in figure 3c, the reconstruction algorithm generates within the mask the main structures of simulation B, which is displayed in figure 2b. This clearly

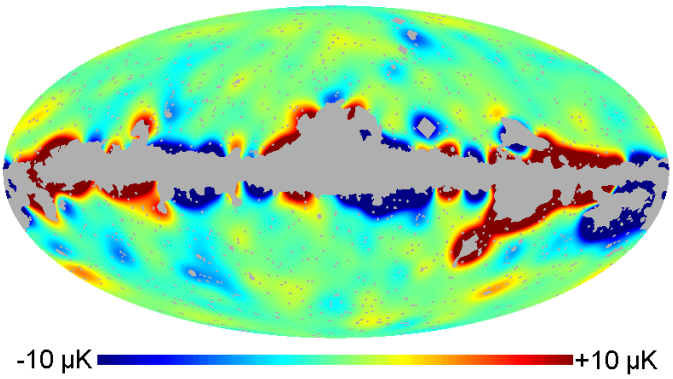

Figure 4. The leak of the ILC temperatures from regions within the mask to those outside due to the smoothing process.

demonstrates the information transfer, so that one has to be careful in testing the reconstruction algorithm. This leads to the question whether the reconstruction can be carried out using only unsmoothed maps where no information about pixels within the mask is encoded outside. However, then stability difficulties arise as shown below.

Another way to demonstrate the flow of information from regions within the mask to those outside the mask, is the following. At first the pixels of the ILC map outside the KQ85 mask are set to zero. Then a subsequent 10° smoothing shows how much information about the ILC pixel values inside the mask leaks to those regions outside. This leak of information is shown in figure 4. It is obvious that the main structures of the ILC map within the mask appear close to the boundary outside the mask.

The paper is organised as follows. In section 2 the reconstruction errors of the CMB temperatures are evaluated outside and inside the masks using different smoothings and different resolutions. The reconstruction method using the covariance matrix is compared with the direct inversion method. In section 3 the influence of the reconstruction method onto the 2-point correlation function $C(\vartheta)$ of the CMB is investigated where the focus is on large scales. An integrated measure of $C(\vartheta)$ serves in section 4 as a further tool to demonstrate the drawbacks of the reconstruction methods. Finally, in section 5 we summarise our results.

2 STABILITY OF THE RECONSTRUCTION

In the last section the quality of the reconstruction method is tested only visually. In order to quantify the accuracy of the method, we start with a temperature map $\delta T_{\rm true}(i)$ which is considered as containing the true temperature information also inside the mask. Here i denotes the index of a pixel within the map. The reconstruction algorithm (3) gets as input only the temperatures of those pixels lying outside the given mask and returns a map $\delta T_{\rm rec}(i, l_{\rm max})$ for all pixels. The resulting map depends on the multipole $l_{\rm max}$ up to which the reconstruction is carried out. The reconstruction accuracy can then be quantified by

$$\Sigma_{\rm rec}(l_{\rm max}) \;=\; \sqrt{\frac{1}{N_m}{\sum_i}' \left(\delta T_{\rm rec}(i, l_{\rm max}) - \delta T_{\rm true}(i, l_{\rm max})\right)^2} \quad , \tag{6}$$

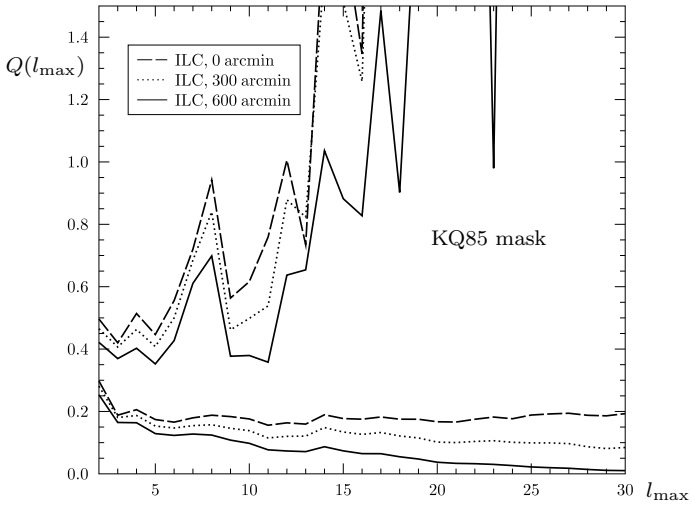

Figure 5. The three upper curves show the normalised total error $Q(l_{\rm max})$ of the reconstruction applied to the ILC (7yr) map using the KQ85 (7yr) mask in dependence on the multipole $l_{\rm max}$. In addition to the original ILC map, the algorithm is applied to smoothed ILC maps with a smoothing of 300 and 600 arcmin at the resolution $N_{\rm side} = 512$. The reconstruction is carried out for the mask threshold $x_{\rm th} = 0.5$ using the resolution $N_{\rm side} = 16$. The three lower curves show the total error $Q(l_{\rm max})$ evaluated for the pixels outside the mask.

where the prime means that the sum is restricted to the N_m pixels within the mask. This gives the average error within the mask. The magnitude of $\Sigma_{\rm rec}(l_{\rm max})$ depends on the normalisation of the map $\delta T_{\rm true}(i, l_{\rm max})$, which is obtained from the original map $\delta T_{\rm true}(i)$ by taking into account only the modes up to $l_{\rm max}$. Note that the expansion $\delta T_{\rm true}(i, l_{\rm max})$ is only possible for full sky maps since a spherical expansion is necessary. To normalise $\Sigma_{\rm rec}(l_{\rm max})$ to a unit fluctuation, the reconstruction accuracy should be measured with respect to the mean temperature fluctuation

$$\sigma_{\rm true}(l_{\rm max}) \;=\; \sqrt{\frac{1}{N_o}{\sum_i}'' \delta T^2_{\rm true}(i, l_{\rm max})} \quad , \tag{7}$$

where the sum with the two primes is restricted to the N_o pixels outside the mask. The normalised total reconstruction error is then given by the quotient

$$Q(l_{\rm max}) \;=\; \frac{\Sigma_{\rm rec}(l_{\rm max})}{\sigma_{\rm true}(l_{\rm max})} \quad . \tag{8}$$

A value of $Q = 1$ means that the error is as large as a typical temperature value, i. e. the reconstruction is useless.

We apply the normalised accuracy measure (8) to the ILC (7yr) map and to simulations of the ΛCDM concordance model where the cosmological parameters of the WMAP team are used (Table 8, column "WMAP+BAO+H_0" in Jarosik et al. (2010)). These maps with a resolution of $N_{\rm side} = 512$ are smoothed to a Gaussian width $\theta = 1°$, and in the following only a smoothing in addition to this $\theta = 1°$ smoothing is given. After the smoothing the maps are downgraded to lower resolutions of $N_{\rm side} = 16$ or 32. Then the downgraded masks are applied in this lower resolution, which gives the maps which serve as the input for the reconstruction algorithm.

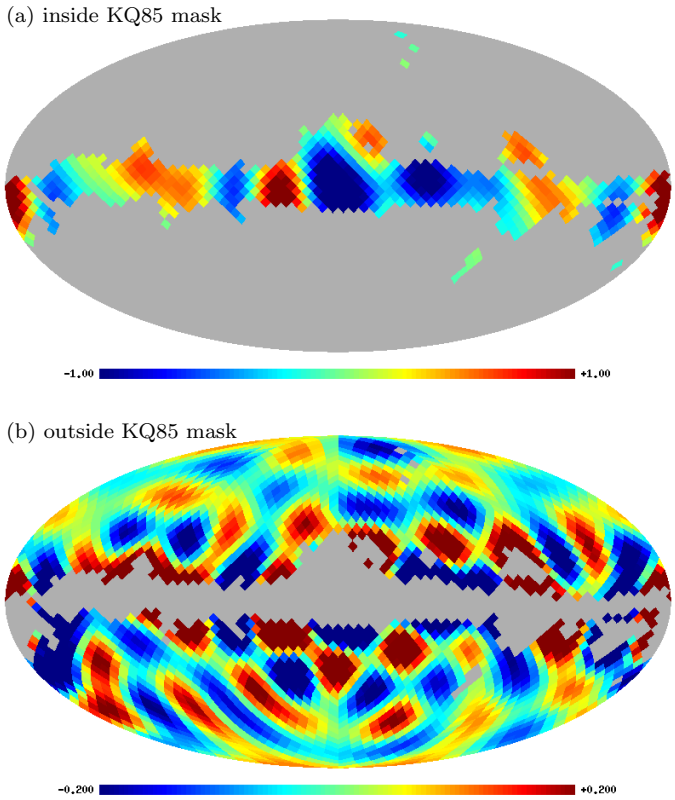

Figure 6. The upper panel shows the local reconstruction error (9) of the ILC (7yr) map within the KQ85 mask corresponding to the total reconstruction error $Q(10) = 0.62$ of the ILC map as can be read off from figure 5 at $l_{\max} = 10$. The colour bar is truncated such that q-values less than -1.0 are pictured as dark blue and larger than 1.0 as dark red. In the lower panel the same quantity is pictured outside the mask. Here typical q-values lie between -0.2 and +0.2 as can be read off in figure 5. For this reason the maximum and minimum values are truncated at 0.2 and -0.2, respectively.

In figure 5 the three upper curves reveal the total reconstruction error (8) for ILC (7yr) map using the KQ85 (7yr) mask for different smoothings. As outlined above the algorithm depends on the multipole $l_{\max}$ up to which the multipoles $l = 0, \ldots, l_{\max}$ are to be reconstructed. The accuracy measure (8) refers to the maps expanded only up to $l = l_{\max}$. Even for very low values of $l_{\max} \lesssim 10$ the total error $Q(l_{\max})$ is above 0.4, i. e. the temperatures reconstructed within the mask differ from the true ones by one half of the mean temperature fluctuations. This demonstrates the accuracy problems of the algorithm. It is seen that the error decreases with increasing Gaussian smoothing because the information leak is getting stronger with increasing smoothing. The three lower curves shown in figure 5 are the total errors outside the mask. These are computed using equation (6) but with the modification that the primed sum runs only over those pixels i outside the mask. It is seen that with increasing value of $l_{\max}$ the accuracy gets better although the error is surprisingly large for small reconstruction multipoles $l_{\max}$. With additional smoothing the total reconstruction error of the ILC map has the tendency to fall, but without additional smoothing the total error is nearly constant about 0.2.

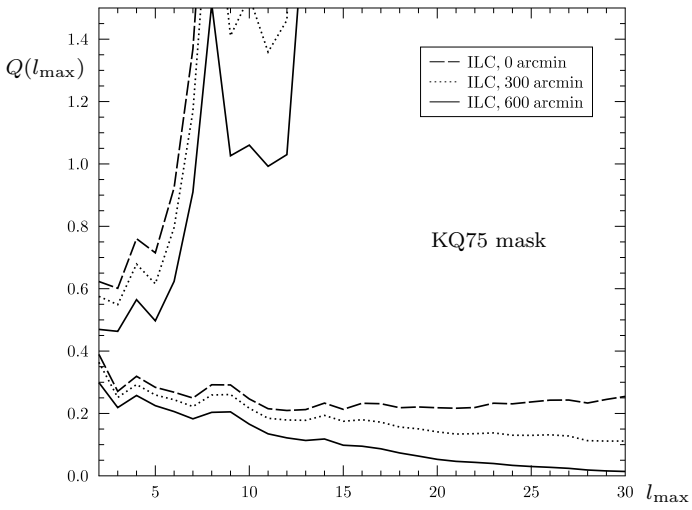

Figure 7. The same analysis for the normalised total error $Q(l_{\max})$ as in figure 5 is presented, but now the larger KQ75 (7yr) mask is used instead of the KQ85 (7yr) mask.

Up to now only the global accuracy measure Q is discussed. But in order to find the regions which are most prone to reconstruction errors, we now introduce the reconstruction accuracy of single pixels which is obtained by taking the difference between $\delta T_{\rm rec}(i, l_{\max})$ and $\delta T_{\rm true}(i, l_{\max})$. Normalising this difference with $\sigma_{\rm true}(l_{\max})$ results in the local reconstruction error

$$q(i, l_{\max}) \;=\; \frac{\delta T_{\rm rec}(i, l_{\max}) - \delta T_{\rm true}(i, l_{\max})}{\sigma_{\rm true}(l_{\max})} \quad . \qquad (9)$$

To expose the regions with the largest errors, the local reconstruction error (9) of the ILC map (without additional smoothing) is pictured in figure 6 for $l_{\max} = 10$. The errors within the mask are shown in figure 6a. In this figure dark areas display errors with $|q| \geqslant 1$. Such values of q occur near the galactic centre where the mask is very extended. But errors larger than 1 also occur antipodal to the galactic centre. The errors outside the mask are shown in figure 6b. Based on figure 5 one would expect that a typical value of the local reconstruction error (9) is about ± 0.2. The colour band is truncated at those values of $|q|$ such that values of $|q| \geqslant 0.2$ are pictured as dark blue or dark red. It is seen that large errors outside the mask appear near the masked region. A further observation is that with increasing $l_{\max}$ the most significant errors approach the masked region. Then the values of the maximum errors increase, although the areas with $|q| \geqslant 0.2$ are getting smaller.

Since the reconstruction error depends on the size of the mask, it is interesting to consider the larger KQ75 (7yr) mask which again is applied to the ILC (7yr) map. In figure 7 the three upper curves display the corresponding total reconstruction errors (8) within the mask. Even for very low values of $l_{\max} \lesssim 5$ the total error $Q(l_{\max})$ is above 0.5, i. e. the temperatures reconstructed within the mask differ from the original ones by more than one half of the mean temperature fluctuation. For $l_{\max} \geqslant 7$ the total error $Q(l_{\max})$ is even above 1.0. It is seen that the error decreases with increasing Gaussian smoothing because of the information

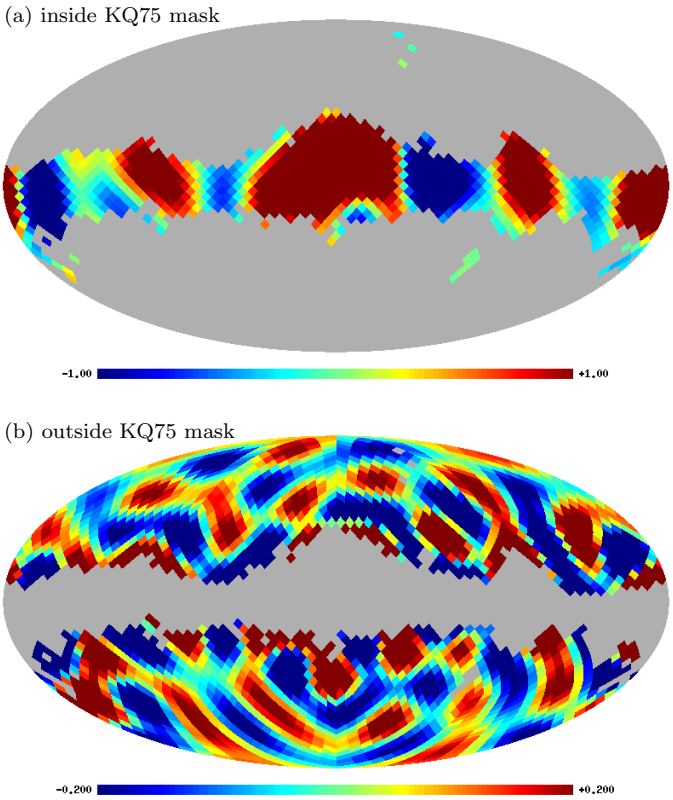

Figure 8. The upper panel depicts the local reconstruction error (9) of the ILC (7yr) map within the KQ75 mask corresponding to the total reconstruction error $Q(10) = 1.86$ as figure 7 reveals at $l_{\max} = 10$. In the lower panel the same quantity is pictured outside the mask. The colour bands are truncated in the same way as in figure 6, i. e. at ± 1.0 and ± 0.2 in the upper and lower panel, respectively.

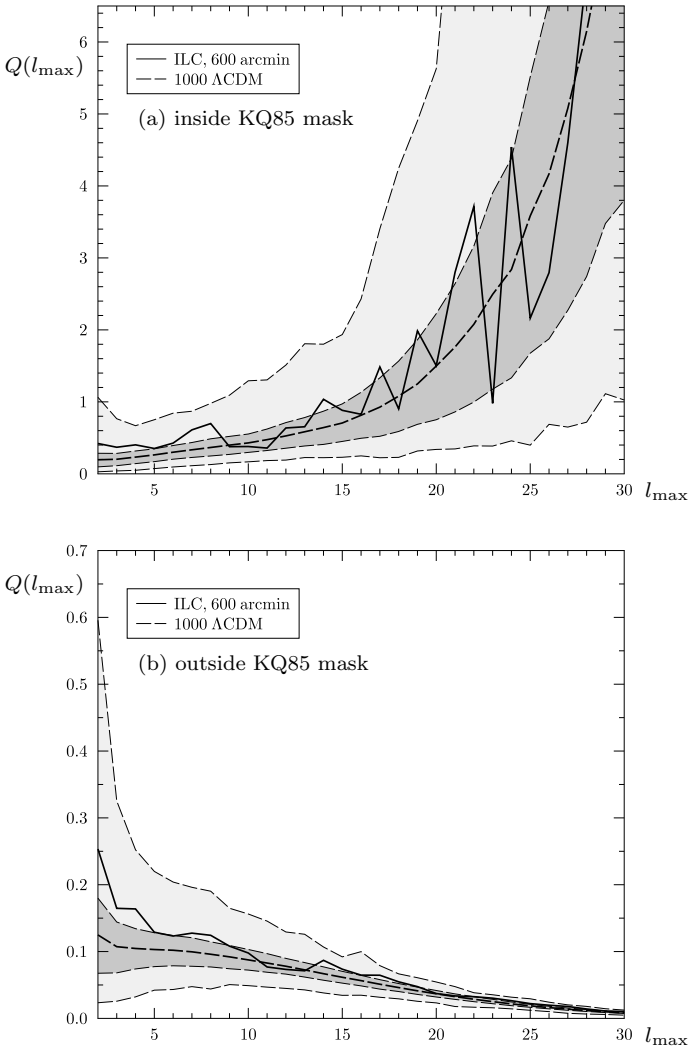

Figure 9. In the upper panel the solid curve shows the normalised total error $Q(l_{\max})$ of the reconstruction inside the KQ85 (7yr) mask applied to the ILC (7yr) map smoothed with 600 arcmin in dependence on the multipole $l_{\max}$. The reconstruction is carried out for the mask threshold $x_{\rm th} = 0.5$ using the resolution $N_{\rm side} = 16$. The mean value of the total reconstruction error calculated from 1000 CMB simulations is displayed as a dashed curve. The range containing 66.6 % of these models is pictured as dark grey band. The distribution of all errors of these 1000 CMB simulations is given as a light grey band. The lower panel shows the corresponding total reconstruction errors outside the mask.

leak, but nevertheless the total error $Q(l_{\max})$ is large for a smoothing with 600 arcmin. The three lower curves shown in figure 7 are the total errors outside the mask. It is seen that with increasing value of $l_{\max}$ the accuracy improves although the error is surprisingly large for small reconstruction multipoles $l_{\max}$. With additional smoothing the total reconstruction error of the ILC map has the tendency to fall, but without additional smoothing the error is nearly constant at about 0.25.

To reveal the locations of the most significant errors in the case of the KQ75 (7yr) mask, the local reconstruction error of the ILC map (without additional smoothing) is pictured in figure 8 for $l_{\max} = 10$. The errors within the mask are shown in figure 8a. The dark areas display errors with $|q| \geqslant 1$ which are much more widespread than for the KQ85 (7yr) mask. The errors outside the mask are shown in figure 8b. To locate large errors we have pictured values of $|q| \geqslant 0.2$ as dark blue or dark red. The errors outside the mask are only slightly larger than in the case of the KQ85 (7yr) mask.

Compared to the KQ85 (7yr) mask, the accuracy problems of the algorithm applied to the larger KQ75 (7yr) mask are much stronger, and we conclude that this mask is too large in order to allow a reconstruction for $l_{\max} \geqslant 7$, and even the results for $l_{\max} < 7$ should be considered critical. For this reason we concentrate us in the following on reconstructions using the smaller KQ85 (7yr) mask.

Now we compare the total reconstruction error of the ILC map with those of 1000 CMB realizations of the ΛCDM concordance model. In figure 9 this comparison is shown with the additional smoothing of 600 arcmin and in figure 10 without smoothing. A resolution of $N_{\rm side} = 16$ and a mask threshold $x_{\rm th} = 0.5$ is used. As can be seen in the upper panel of figure 9 the total reconstruction error of the ILC map within the mask is located for $l_{\max} \leqslant 8$ outside the dark grey band containing 66.6% of 1000 models, but between the maximum and minimum errors of these mod-

els which domain is depicted as the light grey band. For $l_{\max} > 8$ the total reconstruction error of the ILC map is rather typical. It should be noted that the computation of the ILC reconstruction error assumes that the ILC map contains the true values inside the mask which, of course, needs not to be the case. But as the comparison with the light grey band shows, the total reconstruction error is always smaller than the extreme errors that occur among the 1000 simulations. The total reconstruction error from these 1000 models with an additional smoothing of 600 arcmin reveals that the reconstruction of the CMB within the mask is impossible for $l_{\max} \gtrsim 16$. In figure 9b the total reconstruction error of the ILC map outside the mask is compared with those of the 1000 ΛCDM models. For $l_{\max} \leqslant 8$ the total reconstruction error of the ILC map is again outside the dark grey band containing 66.6% of the simulations. Furthermore, with increasing $l_{\max}$ the total reconstruction error outside the mask vanishes if the additional smoothing of 600 arcmin is applied.

Figure 10 displays the total reconstruction error without the additional smoothing of figure 9. The total reconstruction error within the mask of the ILC map and of the 1000 simulations is larger without additional smoothing. With increasing value of $l_{\max}$ the reconstruction of the temperature fluctuations within the mask deteriorates increasingly, such that the reconstruction is doubtful for $l_{\max} \gtrsim 13$. The mean values of the total reconstruction error outside the mask of the 1000 ΛCDM simulations are now nearly independent from $l_{\max}$ at a value about 0.15. The width of the distribution of the total reconstruction error decreases with $l_{\max}$.

Figures 6 and 8 depict the local reconstruction error $q(i, l_{\max})$ for the ILC map, where one has to assume that the ILC map contains the true pixel values within the mask. The locations of extreme values of $q(i, l_{\max})$ without this assumption are obtained from the 1000 ΛCDM simulations. The standard deviation of $q(i, l_{\max})$ calculated from these 1000 models (without additional smoothing) is pictured in figure 11 for $l_{\max} = 10$. The upper panel shows the standard deviation within the mask and the lower one outside the mask. Within the mask the standard deviation is extremely large near the centre of the galaxy where a huge area is masked. In general, one finds that the larger the masked domain is, the larger is the standard deviation of $q(i, l_{\max})$ in the centre of such a domain, and accordingly, the larger is the expected local reconstruction error for an individual map. Outside the mask, extreme standard deviations of $q(i, l_{\max})$ occur near the boundary of the mask. The comparison of the local reconstruction error in figure 6 with this standard deviation shows that antipodal to the centre of the galaxy the local reconstruction error is with about 4σ untypically large. This could be a hint for residual foreground in the ILC map.

The reconstruction error depends also on the resolution of the maps. In order to address this point, figure 12 compares the total reconstruction errors $Q(l_{\max})$ obtained from maps with HEALPix resolutions $N_{\rm side} = 16$ and 32. The distribution of $Q(l_{\max})$ of 1000 CMB simulations as well as the curves belonging to the ILC maps are shown. The maps are smoothed to 600 arcmin and the KQ85 (7yr) mask with a mask threshold $x_{\rm th} = 0.5$ is used. One observes that the reconstruction performs at the higher resolution $N_{\rm side} = 32$ a bit better than at the lower resolution $N_{\rm side} = 16$. This behaviour takes place within and outside the mask in a similar way. As previously discussed, it is important to carry out the reconstruction without a smoothing at intermediate steps. For that reason, figure 13 shows the total reconstruction errors $Q(l_{\max})$ without additional smoothing. Aside from this difference the analysis is the same as in figure 12. Omitting a smoothing procedure leads to an overall increase in the total error $Q(l_{\max})$. In addition, without smoothing the reconstruction at the higher resolution $N_{\rm side} = 32$ performs only marginally better than at the lower resolution $N_{\rm side} = 16$. Thus, reconstructions of CMB maps at higher resolutions $N_{\rm side}$ do not yield a crucial improvement if a smoothing has to be avoided.

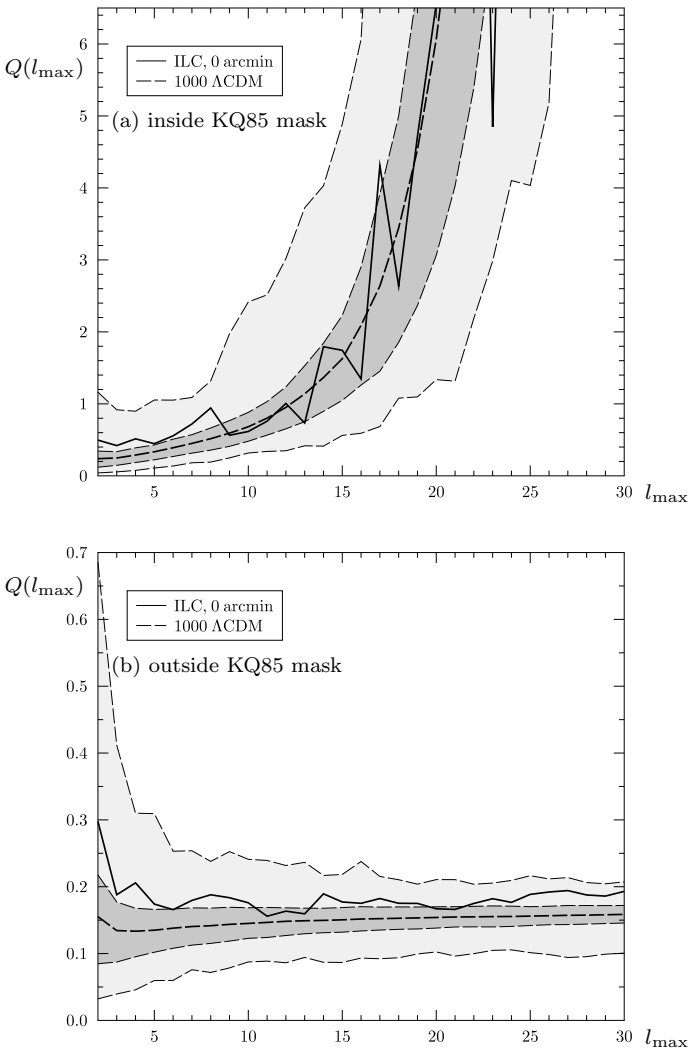

Figure 10. The same analysis of the reconstruction error $Q(l_{\max})$ as in figure 9 is shown, but now without smoothing.

Now we will discuss the influence of the mask threshold $x_{\rm th}$ defined in equation (5). The lower the value of $x_{\rm th}$, the more pixels are excluded in the neighbourhood of the boundary of a masked domain. The total reconstruction errors $Q(l_{\max})$ of 1000 CMB simulations of the ΛCDM concordance model for $x_{\rm th} = 0.1$, 0.5 and 0.9 at a resolution $N_{\rm side} = 16$ (without additional smoothing) are compared

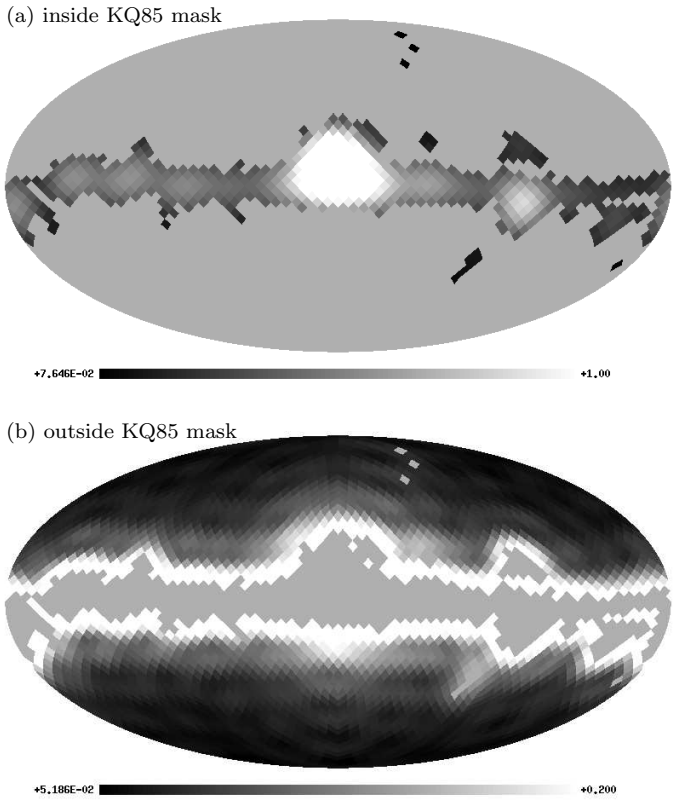

Figure 11. The standard deviation of the local reconstruction error (9) is displayed for $l_{\max} = 10$ calculated from 1000 ΛCDM maps. The upper panel depicts the standard deviation of $q(i, l_{\max})$ within the mask, where values $q \geqslant 1$ are pictured white. In the centre of the galaxy the standard deviation has values as large as 2.12. At the lower panel the same quantity is pictured outside the mask, but now the maximum value is truncated at 0.2. Pixel values larger than 0.4 occur.

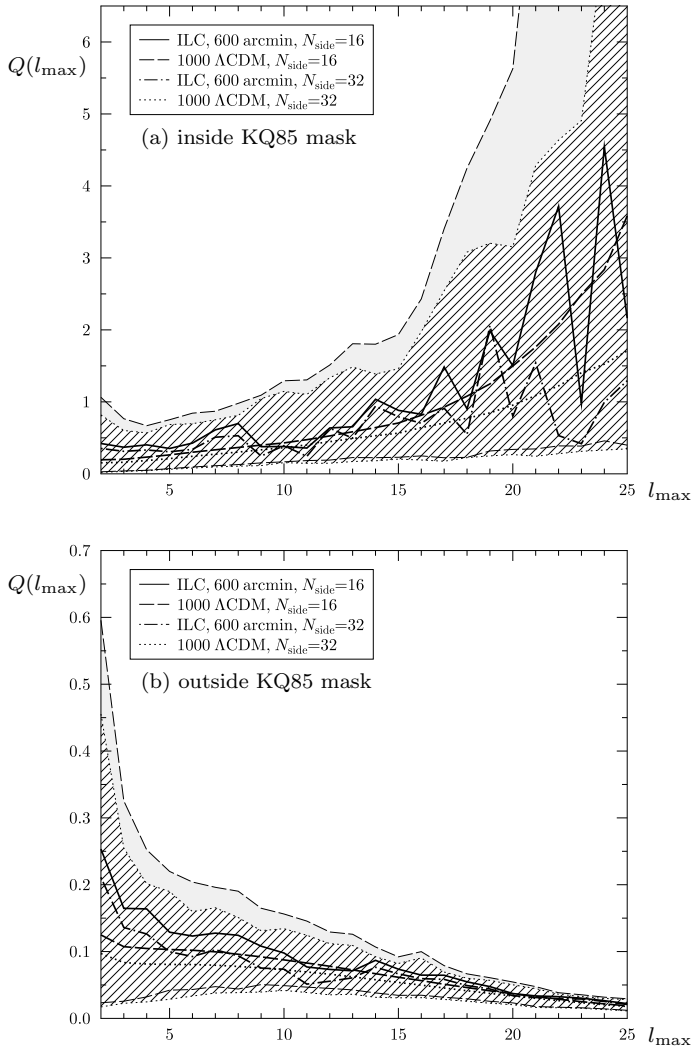

Figure 12. The normalised total error $Q(l_{\max})$ is computed for the two different resolutions of $N_{\rm side} = 16$ and $N_{\rm side} = 32$. The total error $Q(l_{\max})$ is obtained from the ILC (7yr) map together with KQ85 (7yr) mask using a threshold $x_{\rm th} = 0.5$. A smoothing of 600 arcmin is applied. The total error for the ILC (7yr) map for $N_{\rm side} = 16$ is plotted as a solid curve and for $N_{\rm side} = 32$ as a dash-dotted curve. This error is compared with the corresponding mean error obtained from 1000 ΛCDM simulations which is displayed as a dashed curve and as a dotted line, respectively. The distribution of the errors of the 1000 CMB simulations is given as a light grey band and as a shaded band for $N_{\rm side} = 16$ and $N_{\rm side} = 32$, respectively. The upper and lower panels show the total reconstruction errors inside and outside the mask.

in figure 14. For $x_{\rm th} = 0.1$, 0.5 and 0.9 the reconstruction method uses 84.9%, 80.8% and 70.4% of the pixels of a map, respectively. Thus the KQ85 (7yr) mask for $x_{\rm th} = 0.9$ at a resolution $N_{\rm side} = 16$ excludes a region almost as large as the initial KQ75 (7yr) mask, and for $x_{\rm th} = 0.5$ the excluded region is even smaller than the initial KQ85 (7yr) mask. Since the reconstruction accuracy decreases by increasing the mask and because a larger value of $x_{\rm th}$ increases the mask, the reconstruction has more difficulties for larger $x_{\rm th}$ as can be seen in figure 14. One observes in the upper panel that the differences in the total reconstruction errors within the mask for the three thresholds $x_{\rm th}$ are relatively small as long as $l_{\max} \lesssim 5$. But with increasing multipoles $l_{\max}$ the total reconstruction error increases strongly with $x_{\rm th}$. The total reconstruction error within the mask for $x_{\rm th} = 0.1$, 0.5 and 0.9 is typically larger than 1 for $l_{\max} \gtrsim 15$, 13 and 11, respectively. These represents the largest multipoles $l_{\max}$ for which a reconstruction can be carried out in order to avoid constructing random patterns. But for cosmological parameter extractions, even values of $Q(l_{\max})$ near one can be insufficient, since this implies an total error of a typical temperature fluctuation.

Up to now, all reconstructions have used the covariance matrix (4) in equation (3). Thus, we finally compare the reconstruction results by using the covariance matrix with those of the method of direct inversion, where A is the unit matrix. Choosing the unit matrix renders the method independent of an underlying cosmological model, see equation (4). In figure 15 this comparison is carried out for the 1000 ΛCDM simulations using the KQ85 (7yr) mask for a mask threshold $x_{\rm th} = 0.5$ at a resolution of $N_{\rm side} = 16$. The reconstruction using the covariance matrix works better than the method of direct inversion for $l_{\max} \lesssim 8$. For $l_{\max} \gtrsim 9$ the difference between the two methods is marginal. Thus, for

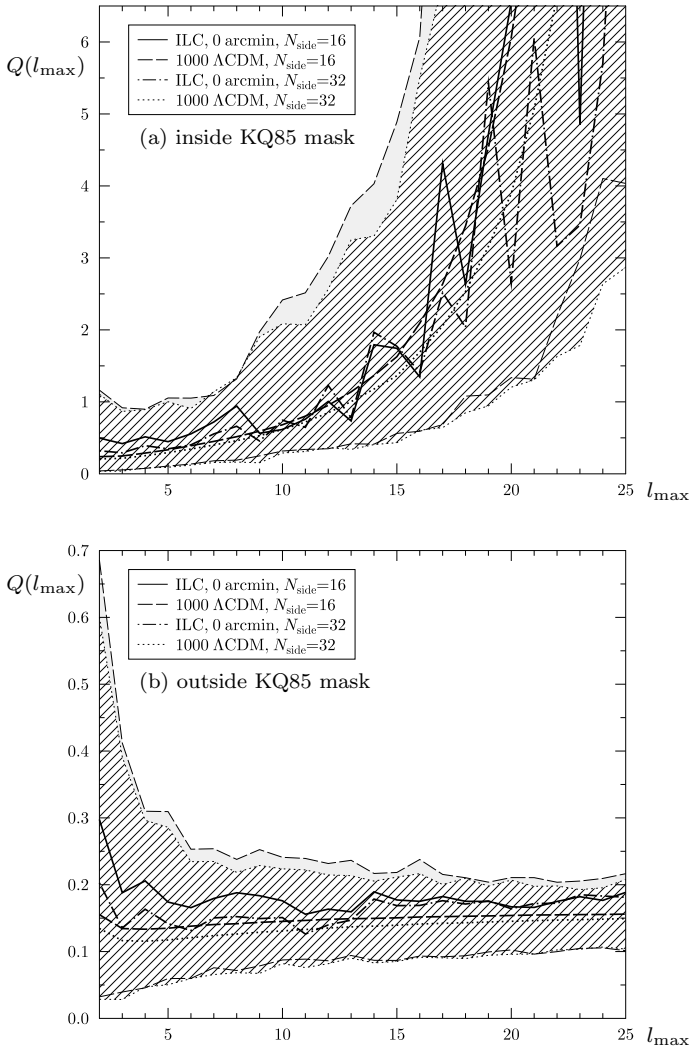

Figure 13. The normalised total error $Q(l_{\rm max})$ is computed from the same data as in figure 12. The sole difference is that no additional smoothing is applied here, which leads to larger values of $Q(l_{\rm max})$ compared to figure 12. Furthermore, a higher resolution leads only to a marginal improvement.

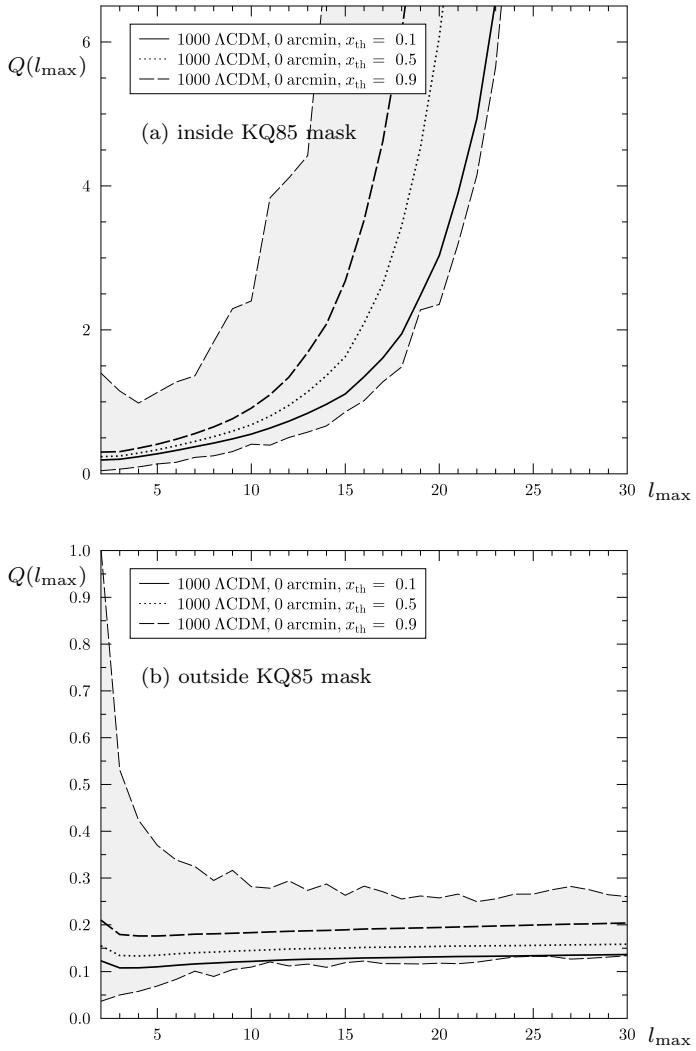

Figure 14. The mean value of the total reconstruction errors $Q(l_{\rm max})$ calculated from 1000 ΛCDM simulations using the KQ85 (7yr) mask for the mask thresholds $x_{\rm th} = 0.1$, 0.5 and 0.9 at a resolution $N_{\rm side} = 16$ are compared. In the case of $x_{\rm th} = 0.9$ the distribution of all reconstruction errors is given as a grey band. The upper and the lower panel show the total reconstruction errors computed within and outside the masks, respectively.

the reconstruction of the lowest multipoles the algorithm using the covariance matrix is preferable, whereas for the larger multipoles the direct inversion can be chosen due to its smaller computational effort. In the case of the method of direct inversion, the mean value of the total reconstruction errors of 1000 simulations at a resolution of $N_{\rm side} = 256$ are also calculated, which does not result in a crucial improvement compared to the reconstruction at a resolution of $N_{\rm side} = 16$. The similarity of both variants of the reconstruction algorithm is due to the fact that the covariance matrix is already nearly diagonal.

The reconstructions of the 1000 ΛCDM simulations and of the ILC map are compared with the multipole expansions of the full initial maps up to the reconstruction value of $l_{\rm max}$. Thus, this comparison stringently needs the full sky map in order to carry out the multipole expansion. In the case of the simulations we know that the full initial maps contain the so-called true CMB temperature fluctuations, and the expansion can be done reliably. The case of the ILC map is more involved since the ILC map contains residual noise and foreground. In particular, within and near the mask one would expect remaining foreground to some extend. The so-called true temperature fluctuations of the ILC map are not necessarily the genuine CMB temperature fluctuations. One has to keep this fact in mind, when one tries to weight the quality of the ILC reconstruction on the basis of the total reconstruction errors $Q(l_{\rm max})$ of the simulations. Thus it is possible that the reconstruction of the CMB of our Universe from the ILC map is even worse than the result in figure 10 suggests.

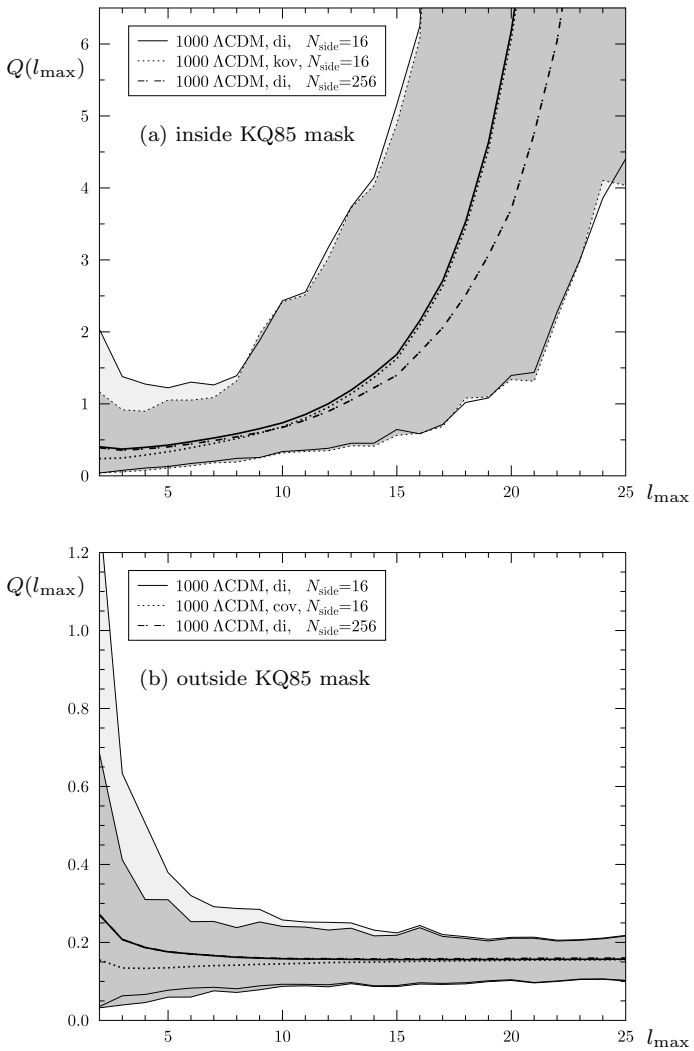

Figure 15. The total errors $Q(l_{\max})$ of the reconstruction using the covariance matrix (4) (cov) are compared with the total errors of the direct inversion (di). Both methods use the KQ85 (7yr) mask with a mask threshold $x_{\rm th} = 0.5$ at a resolution $N_{\rm side} = 16$. The direct inversion is also computed for $N_{\rm side} = 256$. The total error distribution of the 1000 CMB simulations is given as a dark grey band for the algorithm using the covariance matrix and as a light grey band for the direct inversion ($N_{\rm side} = 16$). In the upper panel the total reconstruction errors $Q(l_{\max})$ within the mask are given, and it is seen that for $l_{\max} \leqslant 8$ the covariance method possesses a smaller error distribution. The lower panel shows the corresponding total reconstruction errors outside the mask.

3 CORRELATION FUNCTION $C(\vartheta)$

In this section we address the crucial question whether the sky reconstructions can reliably be used for the estimation of cosmological statistics. The correlation function $C(\vartheta)$ is the suitable statistic with respect to large angular scales ϑ which are relevant for the reconstruction algorithm. This leads to the question of how sensitive the correlation function $C(\vartheta)$, equation (1), varies with respect to the different sky reconstructions. At first one has to determine the minimal value of the reconstruction parameter $l_{\max}$ which is needed for the

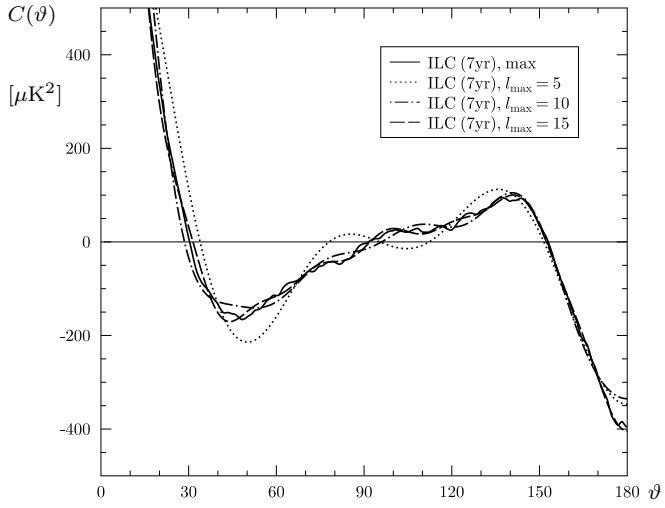

Figure 16. The correlation functions of the full ILC map calculated from the multipoles up to $l_{\max} = 5$, 10 and 15 are compared with the correlation functions of the full ILC map with maximal resolution (max).

reconstructed map in order to give a correlation function $C(\vartheta)$ in agreement with the one obtained from the initial map with full resolution. Therefore, the 2-point correlation functions computed from the multipoles up to $l_{\max} = 5$, 10 and 15 are compared with the correlation function obtained from the full ILC map with maximal resolution in figure 16. From this figure one can read off that at least a reconstruction parameter $l_{\max} \gtrsim 10$ is needed in order to have a good estimation of the correlation function at large scales. The investigations of the previous section lead to the conclusion that the KQ75 mask is already too large in order to allow a reconstruction for such large values of $l_{\max}$. For this reason the following computations are based all on the KQ85 mask with a mask threshold $x_{\rm th} = 0.5$ at a resolution of $N_{\rm side} = 16$. Furthermore, the reconstruction algorithm using the covariance matrix is applied in the following, since it gives for $l_{\max} \gtrsim 10$ almost the same results as the direct inversion method.

In figure 17 three correlation functions $C(\vartheta)$ are shown which are calculated from the reconstructed ILC (7yr) map, from the full ILC map and from the data outside the KQ85 mask. The three panels show the results for the reconstruction parameters $l_{\max} = 10$, 12 and 15. Here the ILC (7yr) map with an additional smoothing of 600 arcmin is used. The reconstructed correlation function is given with 1σ and 2σ deviations of the reconstruction errors which are estimated by

$$\sigma(\vartheta, l_{\max}) := \sqrt{\frac{\sum_{k=1}^{N} (C_{\rm rec}^{(k)}(\vartheta, l_{\max}) - C_{\rm true}^{(k)}(\vartheta, l_{\max}))^2}{N}} \quad , \tag{10}$$

where the index k counts the $N = 1000$ CMB simulations of the ΛCDM model. This quantity takes into account only the error of the reconstruction of pure CMB maps. Additional contributions due to residual foreground and detector noise in the ILC map propagate through the reconstruction algorithm and are not considered here. In all three cases ($l_{\max} = 10$, 12 and 15) the correlation function of the recon-

structed ILC map agrees well within the 2σ errors with the correlation function of the full ILC map and less with the correlation function computed outside the mask. This observation is used by Efstathiou et al. (2009) as an argument in favour of the statement that the "true" correlation function is the one obtained from the full ILC map. However, as already emphasised, the large additional smoothing of 600 arcmin transfers information from the masked region into the data used by the algorithm. For this reason this result is not surprising, and the reconstructed correlation function is very questionable since it is based on the pixels which should have been omitted.

To avoid the problem of information transfer by smoothing the correlation function of the ILC (7yr) map is also investigated without additional smoothing. In figure 18 the corresponding correlation functions are plotted. The error (10) is significantly larger now. Without additional smoothing the differences between the correlation function of the reconstructed and of the full ILC (7yr) map are larger, but both agree within the 2σ errors. This could lead to the conclusion that the reconstruction works without additional smoothing and without a corresponding information transfer, but for $l_{\max} = 10 - 12$ the errors are large compared to the case with additional smoothing as it is shown in figure 17. For $l_{\max} \gtrsim 15$ the errors of the reconstructed correlation function are too large to allow any conclusion. Due to these large errors the correlation function of the reconstructed ILC map also agrees on the same level with the correlation function obtained solely from the data outside the mask. Thus, one cannot differentiate between these two cases. The reconstructed correlation function shows sometimes a better agreement with the correlation function resulting from the masked ILC map and sometimes with the correlation function of the full ILC map. The quality of this agreement depends on ϑ and $l_{\max}$. Thus, the reconstructed correlation function favours neither the one of the masked nor the one of the full ILC map. Due to the large errors the reconstructed correlation function is uncertain by at least $100\mu\mathrm{K}^2$ and thus unsuited for the comparison with cosmological models.

The above discussion puts forward arguments against the reconstruction method and favours methods which use only the data outside a given mask. To provide a firm footing for the latter, the influence of the KQ85 and KQ75 masks onto the ensemble average and the cosmic variance of the correlation function $C(\vartheta)$ is now investigated with respect to the ΛCDM model. Both quantities are shown in figure 19 for an ensemble of 100 000 CMB simulations of the ΛCDM model. The ensemble average and the standard deviation is computed from the correlation functions $C(\vartheta)$ obtained from the data of full maps, outside the KQ85 mask and outside the KQ75 mask. A resolution of $N_{\mathrm{side}} = 128$ and a mask threshold $x_{\mathrm{th}} = 0.5$ is used. The ensemble averages are identical in all three cases. The standard deviation slightly increases with the size of the mask. The smallest 1σ standard deviation is obtained by using no mask at all, the next larger deviation belongs to the KQ85 mask whereas the largest deviation is due to the larger KQ75 mask. The increase of the standard deviation for the masked data is, however, small compared to the uncertainty resulting from the reconstruction method for the same mask. This is a further argument for having more confidence in the correlation function $C(\vartheta)$ computed from the data outside the mask than in the one obtained from a reconstructed full map.

4 THE LARGE ANGULAR SCALE POWER

The main difference between the ILC correlation functions $C(\vartheta)$ computed from the data outside the KQ85 mask and from all pixels is that the former displays much less power at angular scales above 60° than the latter. To describe this observation the $S(60^\circ)$ statistic

$$S(60^\circ) := \int_{-1}^{\cos(60^\circ)} d\cos\vartheta \, |C(\vartheta)|^2 \qquad (11)$$

has been introduced (Spergel et al. 2003), which measures the power on scales larger than 60°. In the following the $S(60^\circ)$ statistic is discussed as a function of the reconstruction parameter $l_{\max}$. At first the results obtained from maps with an additional smoothing of 600 arcmin are presented. In figure 20a the $S(60^\circ)$ statistic is computed from the full ILC map, from the data outside the mask and from the reconstructed ILC map. It is striking to see that in the case of the reconstructed map the $S(60^\circ)$ statistic does not converge to a stable value as it is the case for the full ILC map as well as for the masked ILC map for $l_{\max} \gtrsim 6$. This emphasises the uncertainty of reconstructed maps despite the information transfer by smoothing the map. In figure 20b the mean value of the $S(60^\circ)$ statistic, calculated from 1000 CMB simulations of the ΛCDM model, is displayed again with an additional smoothing of 600 arcmin. As in figure 20a the statistic is plotted for full maps, for reconstructed maps and for masked maps. Since the ΛCDM model has significantly more power at scales above $\vartheta = 60^\circ$, the scale of the ordinate now differs from that of figure 20a. This should be noted by comparing both panels. For $l_{\max} \lesssim 10$ the mean value of the $S(60^\circ)$ statistic of the reconstructed maps differs only marginally from that of the full maps, but for $l_{\max} \gtrsim 10$ the differences are pronounced. If the reconstruction method would work perfectly, the mean values of the $S(60^\circ)$ statistic of reconstructed maps and of full maps should be identical, but there is a systematic overestimation of power in the reconstructed maps. This clearly hints to a systematic error by using the reconstruction method. The overestimation of the mean value of the $S(60^\circ)$ statistic obtained from 1000 simulations again stresses the problems of the reconstruction method for $l_{\max} \gtrsim 10$.

Furthermore, figure 20b reveals that the mean value of the $S(60^\circ)$ statistic increases by 10% by using only the data outside the KQ85 mask compared to the full pixel input. It is interesting to note that the reverse behaviour occurs in the case of the ILC map. There, the $S(60^\circ)$ statistic obtained from the masked map is below that of the full map. Using the above observation based on 1000 simulations, one would rather expect that the $S(60^\circ)$ statistic of the full ILC map should lie 10% below the one of the masked map. The ILC map displays in this respect an untypical behaviour.

In figure 21 the same quantities are displayed as in figure 20, but now calculated without additional smoothing of the maps. Compared to the previous case with smoothing, the $S(60^\circ)$ statistic of the reconstructed ILC map fluctuates even stronger for $l_{\max} \gtrsim 6$ which emphasises the

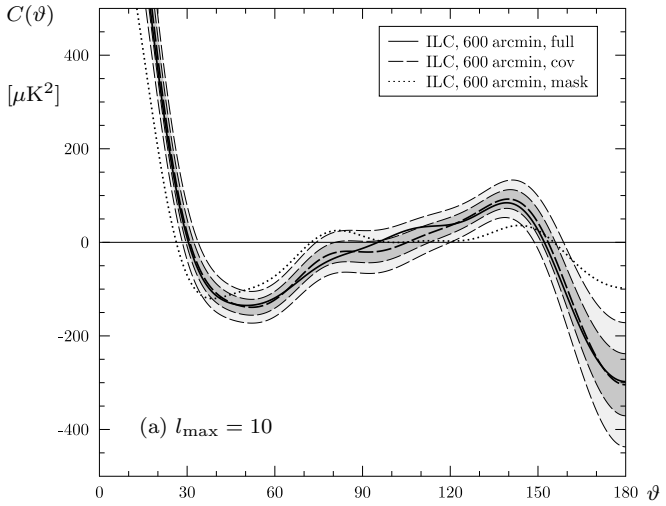

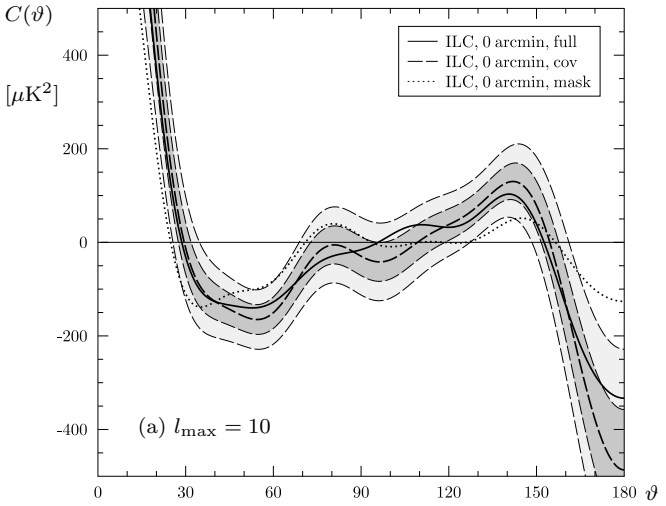

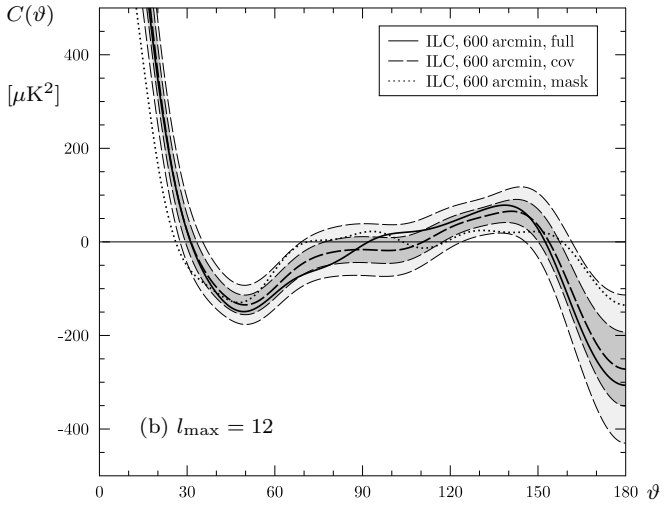

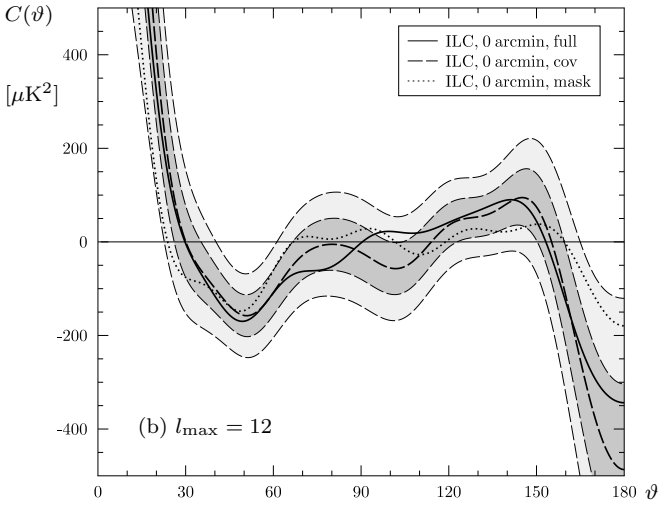

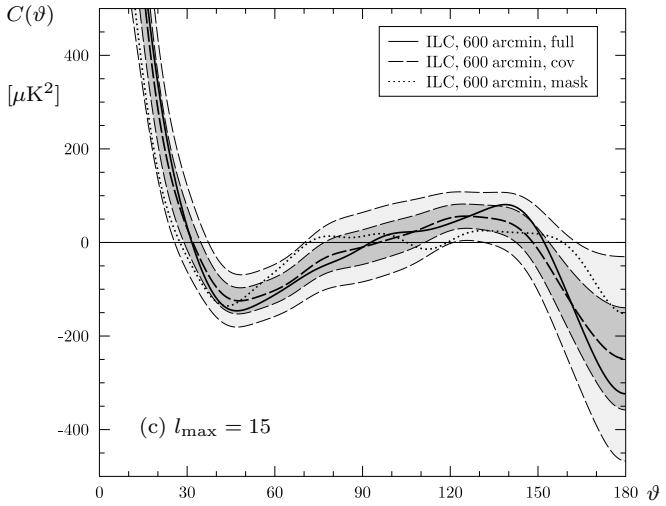

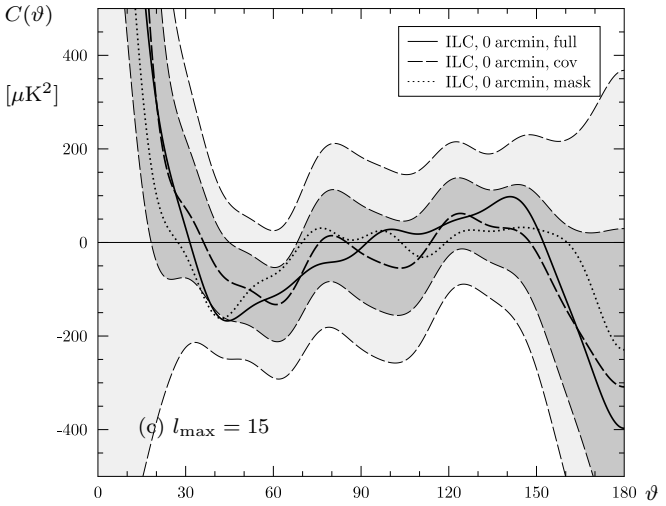

Figure 17. In panel (a), (b) and (c) the correlation function $C(\vartheta)$ of the reconstructed ILC map (cov) is compared with $C(\vartheta)$ of the full ILC map (full) and $C(\vartheta)$ computed outside the mask (mask) for $l_{\max} = 10$, 12 and 15, respectively. Here the ILC map is additionally smoothed to 600 arcmin. The reconstruction is based on the KQ85 mask ($x_{\mathrm{th}} = 0.5$ and $N_{\mathrm{side}} = 16$). The dark grey and light grey band show the 1σ and 2σ band of $\sigma(\vartheta, l_{\max})$, eq. (10), calculated from 1000 ΛCDM simulations, respectively.

Figure 18. The same computations are displayed as in figure 17, but here the ILC (7yr) map is used without additional smoothing which leads to significantly larger errors.

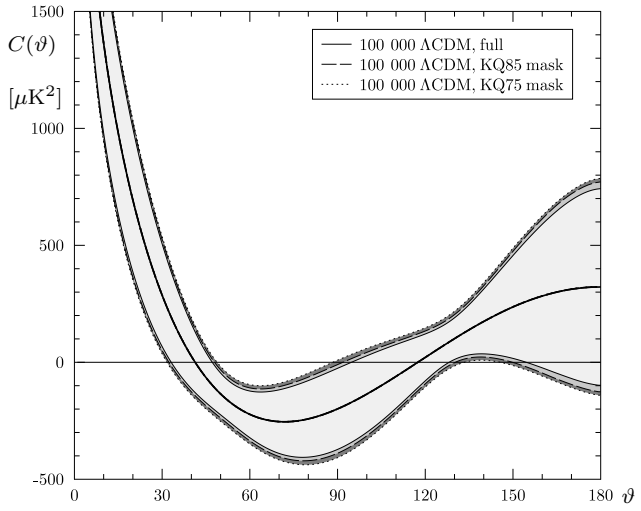

Figure 19. The mean value of the correlation function $C(\vartheta)$ of full maps computed from 100 000 CMB simulations of the ΛCDM model is compared with the mean values of $C(\vartheta)$ using the KQ85 (7yr) mask and the KQ75 (7yr) mask. The mean values cannot be distinguished in this plot. All calculations are carried out with a resolution of $N_{\mathrm{side}} = 128$ and a mask threshold of $x_{\mathrm{th}} = 0.5$. The light grey band gives the 1σ standard deviation calculated from full maps of the 100 000 CMB simulations. The medium grey and the dark grey band correspond to the 1σ standard deviations calculated from the same 100 000 maps, but now outside the KQ85 and outside the KQ75 mask, respectively.

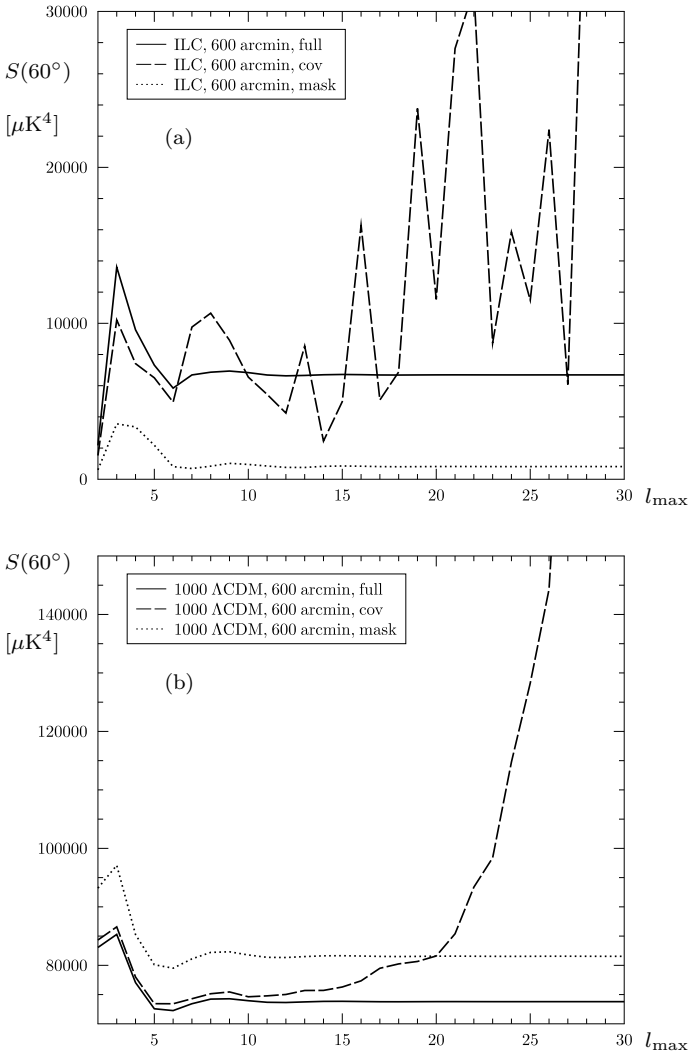

Figure 20. In panel (a) the $S(60°)$ statistic of the reconstructed ILC (7yr) map (cov), the full ILC (7yr) map (full) and the ILC (7yr) map outside the applied mask (mask) is plotted as a function of l_{max}. Here the ILC map is additionally smoothed with 600 arcmin. The reconstruction is carried out applying the KQ85 (7yr) mask for the mask threshold $x_{\mathrm{th}} = 0.5$ using the resolution $N_{\mathrm{side}} = 16$. In panel (b) the mean values of the $S(60°)$ statistic calculated from 1000 CMB simulations of the ΛCDM model are plotted.

strong uncertainty of the reconstruction without the information transfer caused by smoothing. For $l_{\mathrm{max}} > 15$ the $S(60°)$ statistic of the reconstructed ILC (7yr) map yields extremely large values which corresponds to the overestimation of the power of the correlation function at large scales. The mean value of the $S(60°)$ statistic calculated from 1000 CMB simulations of the ΛCDM model is plotted in figure 21b. Again the overestimation of power in the case of reconstructed maps is much more pronounced as in the case without an additional smoothing. Now this overestimation increases very fast already for $l_{\mathrm{max}} \gtrsim 12$ which shows that for these values of l_{max} the reconstructed results definitely contain significant systematic errors. For individual maps the errors can be significant for even lower values of l_{max} as shown in figure 21a for the ILC map.

The figures 20 and 21 also reveal the fact that the low value of $S(60°)$ of the ILC map is rather unusual. As can be read off from the figures this value is much smaller than the mean value due to the 1000 ΛCDM simulations. The $S(60°)$ statistic of the ILC map is now compared with those of 100 000 ΛCDM simulations in order to find the frequency of simulations with even lower power than contained in the ILC map, i. e. which satisfy the condition (Spergel et al. 2003; Copi et al. 2010)

$$S_{\Lambda\mathrm{CDM}}(60°) \; < \; S_{\mathrm{ILC}}(60°) \quad .$$

This condition is satisfied by only 5244, 54 and 16 models out of the 100 000 CMB simulations where $S(60°)$ is computed from data of the full map, outside the KQ85 mask, and outside the KQ75 mask, respectively. As discussed above the values of $S(60°)$ of the ILC map is lower for the masked map than for the full map which is unusual. How unusual this behaviour is, becomes evident by the fact that none of the 100 000 ΛCDM simulations simultaneously satisfy the conditions $S_{\Lambda\mathrm{CDM}}(60°) > S_{\mathrm{ILC}}(60°)$ for data of the full map and $S_{\Lambda\mathrm{CDM}}(60°) < S_{\mathrm{ILC}}(60°)$ for data outside the KQ85 mask. Using instead of the KQ85 mask the KQ75 mask leads to only 2 models out of 100 000 CMB simulations which satisfy both conditions simultaneously. This is a clear hint that the ILC map shows an untypical behaviour compared to the ΛCDM concordance model.

5 SUMMARY

In this paper we have investigated the reconstruction of pixel values within masks using inversion methods. We have com-

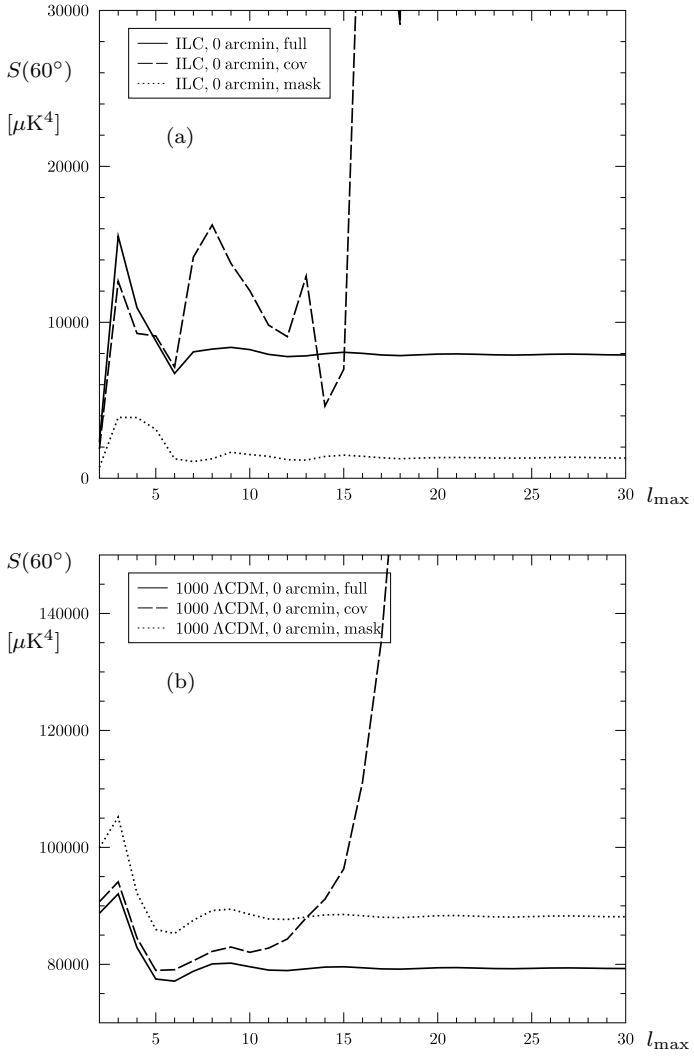

Figure 21. The same quantities as in figure 20 are displayed for the ILC (7yr) map in panel (a) and for 1000 ΛCDM simulations in panel (b), but now they are calculated from the maps without additional smoothing.

pared the algorithm using the covariance matrix with the direct inversion method. The comparison shows that for the reconstruction of multipoles $l_{\max} \lesssim 8$ the algorithm using the covariance matrix gives slightly smaller errors than the direct inversion method. For this reason we focus on the reconstruction method which uses the covariance matrix.

An important point of our analysis is that the additional smoothing of 10° of the ILC map in Efstathiou et al. (2009) transfers information from pixels inside the mask to pixels outside. This should not happen since the pixel values inside the mask are considered as insecure and should be ignored. The smoothing, however, leads to a quantitatively better reconstruction of the ILC map, if the masked domain is considered as containing the true pixel values which have to be recovered by the reconstruction. But the contribution of information from masked pixels makes a reconstructed map obtained from data with additional smoothing unacceptable in a realistic application.

The errors of the pixel values of the reconstructed map are compared with the mean temperature fluctuation $\sigma_{\rm true}(l_{\max})$ defined in equation (7). In the case of the KQ75 (7yr) mask the reconstructed pixels inside the mask have errors larger than $\sigma_{\rm true}(l_{\max})$ already for $l_{\max} \gtrsim 6$ such that the reconstruction is unusable as revealed by figure 7. Even for smaller values of $l_{\max}$ the errors are at least of the order of $\frac{1}{2}\sigma_{\rm true}(l_{\max})$. The culprit for this negative result is the size of the KQ75 (7yr) mask being too large for a reconstruction.

In the case of the smaller KQ85 (7yr) mask the reconstruction without additional smoothing leads for $l_{\max} \gtrsim 13$ to errors larger than $\sigma_{\rm true}(l_{\max})$ such that a rough reconstruction can be done for $l_{\max}$ around 10. However, even with this restriction, errors larger than $\frac{1}{2}\sigma_{\rm true}(l_{\max})$ occur, see figure 5. This might be too large for cosmological applications. It is also checked that refining the resolution from $N_{\rm side} = 16$, which is used in the above computations, to $N_{\rm side} = 32$ does not improve the reconstruction.

Furthermore, the behaviour of the temperature 2-point correlation function $C(\vartheta)$ is analysed with respect to the various reconstructed maps, i. e. with and without additional smoothing, for the ILC (7yr) map and for CMB simulations of the ΛCDM concordance model. The correlation function $C(\vartheta)$ is computed from the full ILC map, from the data outside the KQ85 mask, and from the reconstructed ILC maps which depend on $l_{\max}$. In order to get a good approximation of the correlation function $C(\vartheta)$ on large angular scales, the multipoles up to $l_{\max} \simeq 10$ are needed. The application of the large KQ75 mask is therefore excluded. The errors of the reconstructed 2-point correlation function are estimated by using 1000 CMB simulations of the ΛCDM model. Since this error estimation is based on simulations which contain only the pure CMB signal, no further errors are taken into account e. g. resulting from residual foreground and detector noise. Therefore, the error estimation of the correlation function of the ILC map gives only a lower bound of the errors expected in a genuine application.

As discussed above the reconstructed ILC map with additional smoothing of 600 arcmin uses information from inside the mask. This information transfer leads in turn to underestimated errors in the 2-point correlation function. Furthermore, the similarity of $C(\vartheta)$ computed from the full ILC map and from the reconstructed map is due to this information transfer and not the achievement of the reconstruction algorithm.

Without additional smoothing the ILC correlation function $C(\vartheta)$, computed from the reconstructed map, does not match the one of the full map better than the one of the masked map within the estimated errors. This is caused by the large errors which increase with $l_{\max}$. For $10 \lesssim l_{\max} \lesssim 12$ the reconstructed 2-point correlation function is uncertain by $100\mu K^2$ and for even larger values of $l_{\max}$ useless as revealed by figure 18.

This uncertainty is also reflected in the $S(60°)$ statistic which integrates the power of the 2-point correlation function on angular scales larger than 60°. The $S(60°)$ statistic of the reconstructed ILC map does not converge to a stable value for $l_{\max} \gtrsim 6$ as it is the case for the full and for the masked ILC map as displayed in figure 21a. In addition, the mean value of the $S(60°)$ statistic, calculated from 1000 reconstructed CMB sky maps, reveals the instability of the algorithm for $l_{\max} \gtrsim 12$, where the power strongly increases,

see the dashed curve in figure 21b. This demonstrates the inability to reconstruct the temperature correlations.

The conclusion of this paper is that by using a realistic mask for the WMAP data the reconstruction algorithm (3) does not work well enough to obtain a prediction of the 2-point correlation function. For this reason a cosmological analysis of the WMAP data should use only data outside a mask, e g. the KQ85 (7yr) or KQ75 (7yr) mask. The Planck satellite measures the sky at more different frequencies than the WMAP satellite. This should allow a more secure reduction of the foreground in the CMB map. It is expected that the masked region in the Planck data is significantly smaller. It might be small enough in order to allow an acceptable reconstruction of the CMB within the mask which could provide a 2-point correlation function useable at large scales.

ACKNOWLEDGMENTS

We would like to thank the Deutsche Forschungsgemeinschaft for financial support. HEALPix (healpix.jpl.nasa.gov) (Górski et al. 2005) and the WMAP data from the LAMBDA website (lambda.gsfc.nasa.gov) were used in this work. The computations are carried out on the Baden-Württemberg grid (bwGRiD).

REFERENCES

Aurich, R., Janzer, H. S., Lustig, S., and Steiner, F. (2008). Do we Live in a "Small Universe"? *Class. Quantum Grav.* , 25:125006.

Aurich, R., Lustig, S., and Steiner, F. (2010). Hot pixel contamination in the CMB correlation function? *Class. Quantum Grav.* , 27:095009.

Bennett, C. L., Hill, R. S., Hinshaw, G., Larson, D., Smith, K. M., Dunkley, J., Gold, B., Halpern, M., Jarosik, N., Kogut, A., Komatsu, E., Limon, M., Meyer, S. S., Nolta, M. R., Odegard, N., Page, L., Spergel, D. N., Tucker, G. S., Weiland, J. L., Wollack, E., and Wright, E. L. (2010). Seven-Year Wilkinson Microwave Anisotropy Probe (WMAP) Observations: Are There Cosmic Microwave Background Anomalies? *arXiv:1001.4758 [astro-ph.CO]*.

Bielewicz, P., Górski, K. M., and Banday, A. J. (2004). Low-order multipole maps of cosmic microwave background anisotropy derived from WMAP. *Mon. Not. R. Astron. Soc.* , 355:1283–1302.

Copi, C. J., Huterer, D., Schwarz, D. J., and Starkman, G. D. (2007). Uncorrelated Universe: Statistical anisotropy and the vanishing angular correlation function in WMAP years 1-3. *Phys. Rev. D* , 75:023507.

Copi, C. J., Huterer, D., Schwarz, D. J., and Starkman, G. D. (2009). No large-angle correlations on the non-Galactic microwave sky. *Mon. Not. R. Astron. Soc.* , 399:295–303.

Copi, C. J., Huterer, D., Schwarz, D. J., and Starkman, G. D. (2010). Large angle anomalies in the CMB. *arXiv:1004.5602 [astro-ph.CO]*.

de Oliveira-Costa, A. and Tegmark, M. (2006). CMB multipole measurements in the presence of foregrounds. *Phys. Rev. D* , 74:023005.

Efstathiou, G., Ma, Y.-Z., and Hanson, D. (2009). Large-Angle Correlations in the Cosmic Microwave Background. *arXiv:0911.5399 [astro-ph.CO]*.

Gold, B., Odegard, N., Weiland, J. L., Hill, R. S., Kogut, A., Bennett, C. L., Hinshaw, G., Chen, X., Dunkley, J., Halpern, M., Jarosik, N., Komatsu, E., Larson, D., Limon, M., Meyer, S. S., Nolta, M. R., Page, L., Smith, K. M., Spergel, D. N., Tucker, G. S., Wollack, E., and Wright, E. L. (2010). Seven-Year Wilkinson Microwave Anisotropy Probe (WMAP) Observations: Galactic Foreground Emission. *arXiv:1001.4555 [astro-ph.GA]*.

Górski, K. M., Hivon, E., Banday, A. J., Wandelt, B. D., Hansen, F. K., Reinecke, M., and Bartelmann, M. (2005). HEALPix: A Framework for High-Resolution Discretization and Fast Analysis of Data Distributed on the Sphere. *Astrophys. J.* , 622:759–771. HEALPix web-site: http://healpix.jpl.nasa.gov/.

Hajian, A. (2007). Analysis of the apparent lack of power in the cosmic microwave background anisotropy at large angular scales. *arXiv:astro-ph/0702723*.

Hinshaw, G., Banday, A. J., Bennett, C. L., Górski, K. M., Kogut, A., Lineweaver, C. H., Smoot, G. F., and Wright, E. L. (1996). Two-Point Correlations in the COBE DMR Four-Year Anisotropy Maps. *Astrophys. J. Lett.* , 464:L25–L28.

Jarosik, N., Bennett, C. L., Dunkley, J., Gold, B., Greason, M. R., Halpern, M., Hill, R. S., Hinshaw, G., Kogut, A., Komatsu, E., Larson, D., Limon, M., Meyer, S. S., Nolta, M. R., Odegard, N., Page, L., Smith, K. M., Spergel, D. N., Tucker, G. S., Weiland, J. L., Wollack, E., and Wright, E. L. (2010). Seven-Year Wilkinson Microwave Anisotropy Probe (WMAP) Observations: Sky Maps, Systematic Errors, and Basic Results. *arXiv:1001.4744 [astro-ph.CO]*.

Pontzen, A. and Peiris, H. V. (2010). The cut-sky cosmic microwave background is not anomalous. *arXiv:1004.2706 [astro-ph.CO]*.

Sarkar, D., Huterer, D., Copi, C. J., Starkman, G. D., and Schwarz, D. J. (2010). Missing Power vs low-l Alignments in the Cosmic Microwave Background: No Correlation in the Standard Cosmological Model. *arXiv:1004.3784 [astro-ph.CO]*.

Spergel, D. N., Verde, L., Peiris, H. V., Komatsu, E., Nolta, M. R., Bennett, C. L., Halpern, M., Hinshaw, G., Jarosik, N., Kogut, A., Limon, M., Meyer, S. S., Page, L., Tucker, G. S., Weiland, J. L., Wollack, E., and Wright, E. L. (2003). First-Year Wilkinson Microwave Anisotropy Probe (WMAP) Observations: Determination of Cosmological Parameters. *Astrophys. J. Supp.* , 148:175–194.